Journal of the Meteorological Society of Japan

EARLY ONLINE RELEASE

The DOI for this manuscript is
DOI:10.2151/jmsj.2021-069
J-STAGE Advance published date: August 12th, 2021
The final manuscript after publication will replace the preliminary version at the above DOI once it is available.

Cross validation of the network of ground-based radar with GPM during the Remote sensing of Electrification, Lightning, And Mesoscale/microscale Processes with Adaptive Ground Observations (RELAMPAGO) field campaign

Ivan Arias and V. Chandrasekar

1373, Campus Delivery
Colorado State University, Fort Collins, USA

July 31, 2021

Corresponding author: Ivan Arias, 1373 Campus Delivery, Colorado State University, Fort Collins, CO 80523, USA.
E-mail: idariash@colostate.edu

Abstract

The cross validation of the radars in a network is important to make consistent retrievals across the domain and to assure the quality of the products. During the RELAMPAGO field campaign, two C-band radars namely CSU-CHIVO (Colorado State University C-band Hydrological Instrument for Volumetric Observations) and CSAPR-2 (C-band Scan ARM Precipitation Radar) were deployed near the Sierras de Cordoba in Argentina, a region that is known for having some of the most intense severe weather in the world. In addition to these two radars, the operational radar of the Cordoba City namely RMA-1 (Radar Meteorológico Argentino 1) adds another instrument to the RELAMPAGO network. This paper presents an intercomparison study between the RELAMPAGO C-band radars using the GPM spaceborne radar as common reference. A method to bring ground-based radars into better agreement is also proposed. Moreover, the attenuation correction for C-band radar is studied in the context of intercomparing two radars. The attenuation coefficients were computed for the RELAMPAGO domain using local disdrometers deployed during the campaign. After conducting attenuation correction, CSU-CHIVO, CSAPR-2 and RMA-1 compare well with GPM-DPR with a high correlation and bias less than 1dB.

Keywords RELAMPAGO; GPM; CHIVO; CSAPR; ground validation; precipitation measurement

1. Introduction

The RELAMPAGO was a field campaign that took place near the Sierras de Cordoba (SdC) in Argentina. TRMM (Tropical Rainfall Measuring Mission) observations indicate that the SdC have some of the most intense severe weather on the planet (Zipser et al. 2006). Details about TRMM can be found in Kummerow et al. (1998). RELAMPAGO brought to Argentina a dense network of ground-based sensors to investigate deep convection. The word Relampago stands for lightning in Spanish, the primary language spoken in South America.

The SdC have raised the interest of scientists motivated by its storms' strength and characteristics. Since the study presented by Zipser et al. (2006), satellite observations have been used to study the weather near the SdC. For instance, Rasmussen and Houze (2011) uses TRMM and GOES-12 to characterize the type of convection in that region. They also studied the vertical structure of wide convective cores using the precipitation radar on board TRMM. Details about the precipitation radar on board TRMM can be found in Kozu et al. (2001). In Rasmussen and Houze (2016), the authors also use satellite observations to hypothesize the key ingredients for convection initiation near the SdC.

Satellite observations have helped to elucidate the storm's characteristics that lead into such severe weather near the SdC. Nevertheless, ground observations were still needed to complete the picture. The RELAMPAGO field campaign was also motivated by the fact that the SdC can be used as a natural laboratory to further our understanding of deep convection.

RELAMPAGO brought an interdisciplinary group of scientists and many sensors to Argentina. Two C-band radars were deployed near the SdC to investigate the terrain influence on deep convection. The operational radar of Cordoba City adds another instrument to the network of fixed radars that were collecting dual-polarization observation during RELAMPAGO.

RELAMPAGO took place during the austral warm season of 2018. It had an intense observation period (IOP) from November to December of 2018. The campaign also had an extended period (EOP) in January of 2019. During both observation periods, Global Precipitation Mission (GPM) core observatory made several overpasses over the SdC. With the dense network of ground-based sensors deployed during the campaign, RELAMPAGO provides a valuable opportunity for GPM ground validation. Details about GPM mission can be found in Skofronick-Jackson et al. (2017); Hou et al. (2014).

In this paper, we provide a comprehensive analysis evaluating the ground-based radar (GR) during RELAMPAGO using the Dual-frequency Precipitation Radar (DPR) on board the GPM core observatory. Moreover, DPR is used as a common platform between the GRs to see if it can be used to bring them into better agreement. Besides, the comparison of the GRs with DPR is used as an evaluation of the attenuation correction procedure used for the C-band radars. Details about DPR can be found in Kojima et al. (2012); Iguchi (2020); Masaki et al. (2020); Seto et al. (2021)).

This paper is organized as follows. Section 2 describes the network of GRs deployed during RELAMPAGO. It also presents an overview of the GPM DPR overpasses during the campaign, and it discusses important aspects of the data analysis. Section 3 explains the procedures to compare the GRs between themselves and with DPR. It also presents some considerations regarding the limitations of the procedures. Section 4 shows the results of the comparisons between the different platforms. We also present a procedure to compute a more consistent bias between the network of radar. Section 5 offers a discussion of the results and Section 6 our conclusions.

2. The RELAMPAGO radar observation

In this section, we describe the radars used in our study and the GPM DPR overpasses during the RELAMPAGO campaign. The attenuation correction procedure to compensate the C-band reflectivity is also explained.

2.1 The network of C-band radar

Three C-band radars in the RELAMPAGO domain are used in this study. These radars were collecting data during the IOP and the EOP. CSU-CHIVO and CSAPR-2 were brought to Argentina, and they were deployed near the SdC. The RMA-1 is the operational radar of the Cordoba City. All of them are C-band radars with dual-polarization capabilities. Fig. 1

CSU-CHIVO is a research radar from Colorado State University (CSU). Figure 1 shows a picture of CSU-CHIVO deployed South of Cordoba City. CSU-CHIVO started operating on November 10th, 2018, and it was scanning until January 31st, 2019. Fig. 2

CSAPR-2 was deployed as part of the CACTI (Clouds, Aerosols, and Complex Terrain Interactions) project. CACTI is a RELAMPAGO's sister project funded by the US Department of Energy (DOE). CACTI brought many sensors to Argentina to study orographic clouds and their representation in multi-scale models. RELAMPAGO and CACTI overlapped in time, and both deployed sensors near the SdC. Figure 2 shows CSAPR-2 radar, which is located by the radome on the top of the containers. As can be seen in Fig. 2, the CSAPR-2 site also contains other atmospheric sensors such as wind profiler, and cloud radar. Fig. 3

Figure 3 shows the location of the GRs used in this study. CSU-CHIVO is located at 31.63° S latitude, 64.17° W longitude, and 421 m altitude above mean sea level (AMSL); CSAPR-2 coordinates are 32.13° S latitude, 64.73° W longitude, and 1,141 m altitude AMSL; RMA-1 is at 31.44° S latitude, 64.19° W longitude, and 484 m altitude AMSL.

In this study we will denote CSU-CHIVO by CHIVO, CSAPR-2 by CSAPR and RMA-1 by RMA for simplicity of notation.

CHIVO and CSAPR are approximately 80 km apart, whereas CHIVO and RMA are around 25 km. The distance between RMA to CSAPR is approximately 120 km.

2.2 Attenuation correction for the ground radars

C-band reflectivity needs to be corrected for attenuation for quantitative analysis (Bringi and Chandrasekar, 2001). Therefore, the measured reflectivity (Z_m) can be lower than the intrinsic reflectivity (Z), especially in precipitation.

In dual-polarization radars, the specific differential phase (K_{dp}) can be used to account for attenuation. K_{dp} is related to the volume's liquid water content. The following equation shows an estimation of the attenuation using K_{dp} (Bringi and Chandrasekar, 2001):

$$A_H = \alpha K_{dp}^{b} \,, \tag{1}$$

where A_H is the attenuation in the horizontal channel, and α, b are the reflectivity attenuation coefficients.

Taking into account the attenuation, the measured and the intrinsic reflectivity at a range r can be express in dB as:

$$Z_m(r) = Z(r) - 2\int_0^r A(S)dS\,, \tag{2}$$

where the factor two in the integral means that the attenuation is accounted twice since the signal gets attenuated in both directions, from the radar to the target and vice versa. Replacing Eq. (1) in (2) and assuming $b = 1$, it yields that:

$$Z_m(r) = Z(r) - 2\alpha\int_0^r K_{dp}(S)dS. \tag{3}$$

Since K_{dp} is the derivative of the differential phase Φ_{dp} along with the range, Eq. (3) can be expressed as:

$$Z_m(r) = Z(r) - 2\alpha[\Phi_{dp}(r) - \Phi_{dp}(0)]. \tag{4}$$

Thus, the intrinsic reflectivity can be estimated as:

$$Z(r) = Z_m(r) + 2\alpha[\Phi_{dp}(r) - \Phi_{dp}(0)]. \tag{5}$$

The coefficient α can be computed using scattering simulations. Given a drop size distribution (DSD), one can simulate K_{dp} and A_H, with K_{dp}

in deg/km and A_H in dB/km. The slope from a linear regression with intercept in the origin would be the α-value. The DSD can be simulated with a Gamma distribution or it can be measured by disdrometer.

In Bringi and Chandrasekar (2001), the value of α for C-band is reported as 0.073. This value was computed by averaging scattering simulation of a wide variety of Gamma DSD. They also varied the simulations' temperature from 0 to 30°C and took the average to compute the α-value.

We derive the α-value from measured DSD using data from the DOE 2-dimensional video-disdrometer deployed near CSAPR during the campaign (Bartholomew, 2020). The scattering simulations from DSD collected during November and December of 2018 are computed. The simulations are done using the T-matrix procedure and a temperature of 10°C. An α-value of 0.15 was found for the C-band scattering simulation of the measured DSD.

In the rest of the paper, we will refer to the RELAMPAGO coefficients to the one computed using the local disdrometer deployed during RELAMPAGO. We will refer to the global average coefficients to the one reported in Bringi and Chandrasekar (2001).

2.3 Overview of GPM overpasses

TRMM provided the observation to point out the SdC as a natural laboratory to further our understanding of deep convection. However, by the time of the campaign, TRMM mission ended. Nevertheless, its successor, GPM was capturing many interesting cases in different precipitation regimes with dual wavelength capability.

Table 1 shows a list of GPM DPR overpasses during RELAMPAGO with significant weather. The December 6th and January 13th overpasses cover CHIVO domain while the January 31st overpass covers CSAPR domain. The December 6th overpass also covers the RMA domain. Table 1

An RHI (Range Height Indicator) taken during an overpass provides a valuable opportunity for vertical analysis. An RHI observes a vertical cross-section of the storm seen by a radar. During RELAMPAGO, CHIVO and CSAPR scan strategy included RHI. Fig. 4

On December 6th, 2018, the CHIVO RHI along 315° azimuth overlaps significantly well with DPR Ku-band (KuPR) along angle bin 39. Figure 4a shows the location of this RHI in solid line, and the KuPR angle bin 39 in dashed line. Figure 5 shows a vertical section from both platforms. Note that the vertical structure of the storms shows similar patterns, adjusting for their respective resolutions. For instance, the bright band is located at around 2.5 km elevation. Fig. 5

On January 13th, 2019, GPM DPR captured a group of convective cells over CHIVO domain. CHIVO RHI in azimuth 192° overlaps significantly well with KuPR angle bin 13. Figure 6 shows a vertical cross-section of the storm from DPR (Fig. 6a), and CHIVO (Fig. 6b). The solid and the dashed line in Fig. 4b represents the location of the RHI and the KuPR angle bin respectively for this case. Figure 6a.i shows KuPR reflectivity whereas Fig. 6a.ii shows the Dual Frequency Ratio (DFR). The DFR is computed from the DPR Ku and Ka equivalent reflectivity (Z_e).

CHIVO observations for January 13th, 2019 case are shown in Fig. 6b. Note that the core of the cell, located at 65 km from CHIVO and at latitude -32.2 for DPR, exhibits interesting features. Reflectivity is significantly high below 8 km for both platforms, and the column has a remarkable high DFR that coincides with high K_{dp} and differential reflectivity. Hydrometeor classification from CHIVO shows heavy rain below 5 km for this column. Fig. 6

GPM DPR did not have overpasses in the CSAPR domain during the IOP. However on January 31st, 2019, GPM DPR recorded an overpass with CSAPR while one of deep convective cells was in the radar domain. Figure 7 shows a 3D depiction of KuPR reflectivity collected over CSAPR domain. The dashed line in Fig. 4c and Fig. 7 correspond to KuPR angle bin 37. Note from Fig. 7 that the storm is very deep and localized. Fig. 7

3. Inter comparison of the RELAMPAGO network of ground-based radars with GPM

This section describes the methods to compare the radars in the RELAMPAGO network between themselves and with DPR. The cross-comparison is done using the KuPR radar. The term precipitation radar (PR) in this paper will refer to a radar on board a space aircraft to measure precipitation. The methodology to cross-compare a PR with a GR is explained first, and some considerations are analyzed in terms of the resolution and how it can affect the results. Finally, a simple method to inter-compare the ground-based radar is proposed.

3.1 Cross-comparison with GPM

Quantitative comparison between DPR on board the GPM core observatory and GRs is challenging. Many aspects need to be considered, such as time and space alignment.

In terms of time alignment, when the GPM core observatory passes over the domain of a GR, their time difference needs to match well to obtain valid results. The GPM core observatory orbits the earth at a speed of 7 km/s (Skofronick-Jackson et al. 2017). At this pace, The GPM core observatory covers the domain of a GR in approximately 30 seconds. While, it takes a few minutes for a GR to scan its domain fully. Therefore, an overpass close to the middle of the start and end time of a GR scan is desired.

The GRs under consideration have a beam-width of around one degree. At 60 km in range, the vertical resolution of a GR with this characteristic would be about 1 km. In the case of DPR, Kanemaru et al. (2020) shows with real data that the beam-width of KuPR is about 0.72 degrees. With this beam-width and measuring precipitation at around 400 km, KuPR has a footprint of approximately 5 km.

The pulse duration is related to the range resolution of a radar. The range resolution tells what is the vertical and horizontal resolution for a PR and a GR respectively. Since a PR is scanning from the space, the range resolution indicates the vertical resolution in the data. Differently, for a GR, the range resolution designates the horizontal resolution. Table 2

Table 2 shows a summary of the PR and the GRs resolution used in this study. As can be seen in the table, the PR and the GRs have better range resolution than a footprint. However, since both platforms observe the weather from different perspectives, those variables represent different quantities in their data.

Due to the difference in their geometries, a volume matching is needed to cross-compare DPR and a GR. Besides, since the spaceborne radar is moving, it can have issues related to its orbits such as roll, pitch and yaw. Most of these issues have been addressed for TRMM by Bolen and Chandrasekar (2003). In addition, Bolen and Chandrasekar (2000) and Anagnostou et al. (2001) have analyzed extensively the techniques to compare the ground and space borne radar. As a legacy from TRMM, these methods can be used for DPR.

For volume matching, the tools developed by Bolen and Chandrasekar (2003) and implemented by Schwaller and Morris (2011) are used. This algorithm matches both platform data per each GR sweep. It takes the projection of the PR beam in the GR sweep. Then, it averages the gates along the PR beam that intersect with the GR sweep in the vertical. For the GR, it averages all the gates in azimuth and range that intersect with the PR beam. This procedure is done for each GR sweep and then for each PR beam. In this way, the algorithm computes the average reflectivity for the matched volumes.

While very practical, the procedure in Schwaller and Morris (2011) has some limitations regarding the spatial distribution of the storm and the resolution of each platform. The volume matching is done using the coarsest resolution for each platform, i.e., the PR horizontal resolution (5 km) and the GR vertical resolution (1 km). This has many implications when comparing both platforms. For example, in the edges of the storm, non-uniform beam filling can affect the PR approximation with respect to the GR. On the other hand, rapid changes in the vertical structure of the storm, such as in the melting layer or in convection, can affect the GR approximation with respect to the PR. Nevertheless, good results have been obtained using Schwaller and Morris (2011) procedure.

Previous studies have compared GRs with space-borne radars individually. For instance, Biswas and Chandrasekar (2018) compares the reflectivity from DPR with GRs in different precipitation regimes. The GRs used by Biswas and Chandrasekar (2018) are part of the USA's NEXRAD network, and they are located in different cities. Similarly, other studies such as the one presented by Warren et al. (2018) have used space-borne radars as a reference to calibrate GRs situated in different Australian cities. In addition, Louf et al. (2019) uses comparison with DPR to derive absolute calibration for GR reflectivity.

The evaluation of GRs measurement with other measurements from the ground is important when comparing GRs with space-borne radars. The reason is that one can understand better the error structure. It also provides more insight into whether biases are from the cross-comparison with the space-borne radar or inherent to the GRs measurement. A good solution can be to compare a GR with another GR. However, the GRs need to be located nearby.

3.2 *Inter-comparison of ground radars*

The network of GRs deployed during the RELAMPAGO campaign is very valuable for GPM ground validation. A dense network of radar was placed in a relatively small domain. As a result, the radars can be compared between them. In this study, we inter-compare each of the C-band radars deployed during RELAMPAGO with one another.

The inter-comparison of the radars is done by creating a common Cartesian grid. The origin of the grid is selected to be in the middle of the GRs to be compared. The reason is that it equally compensates for variation in the volume for each radar. A widespread stratiform case is used since it provides more stable conditions in terms of the storm variability.

The grid size is chosen to be 16 km square. The vertical extent of the grid is 1.2 km. The horizontal resolution is selected to be the CHIVO range resolution, i.e., 150 m. While the vertical resolution is chosen to be 600 m.

Only data below the melting layer is used. The reason is that the melting layer introduces variabilities to the comparison due to strong spatial gradients. The melting layer is found using RHIs scan from CHIVO. In addition, only data above 1.2 km AMSL is used to avoid ground clutter. Since the grid vertical extend is 1.2 km, precipitation from 1.2 to 2.4 km AMSL is used to compared two GRs.

On November 30th, 2018, at around 3:30 UTC there was a widespread stratiform that covers the GRs' domain. Data acquired around this time is used to perform the inter-comparison. Figure 8 shows CHIVO reflectivity for this case. Note from the RHI in Fig. 8b that the melting layer is located around 2.5 km above the ground level (AGL). Fig. 8

The metrics used to compare the reflectivity of a pair of radars are the bias, Pearson correlation coefficient (CORR), and the root mean square error (RMSE). They are defined respectively in the following set of equation:

$$\text{BIAS} = E[Rd_X - Rd_Y]\,, \tag{6a}$$

$$\text{CORR} = \frac{Cov(Rd_X, Rd_Y)}{\sigma_{Rd_X}.\sigma_{Rd_Y}}\,, \tag{6b}$$

$$\text{RMSE} = E[(Rd_X - Rd_Y)^2]^{1/2}\,, \tag{6c}$$

where $E[.]$ is the expected value, Rd_X is the radar X and Rd_Y the radar Y. $Cov(.)$ is the co-variance and σ_R the standard deviation.

4. Results of the inter-comparison of the RELAMPAGO network of radar with GPM

Comparisons between the radars in a network is important to make consistent retrievals across the study domain. This verification assures the quality of the results and provides a more solid background for quantitative observation. In this section, we inter-compare the GRs deployed during RELAMPAGO. We use DPR as a common platform across the radars in the network. Error and bias are also computed based on DPR comparison.

4.1 Cross-comparison of the ground-based radar with GPM

To compare the RELAMPAGO GRs with GPM DPR, we initially perform attenuation correction to the reflectivity of each GR. The attenuation is estimated using the K_{dp} relationship stated in the Eq. (1). The global average value of the coefficient α in this equation is reported by Bringi and Chandrasekar (2001) as 0.073. However, we obtained a higher value of α (0.15) using local disdrometers deployed during the campaign.

The difference in the RELAMPAGO and the global average coefficient leads into the question of which value shall be used to correct the RELAMPAGO GR reflectivity. To answer this question, we perform attenuation correction to the CHIVO reflectivity using each coefficient separately. Then, the corrected reflectivity is compared with the KuPR reflectivity. It is worth noting that we use the KuPR corrected reflectivity available in the level 2A data set as the PR reflectivity. Figure 9 shows the cross-comparison of CHIVO with DPR for the overpass on January 13, 2019. Fig. 9

Figure 9a shows the comparison using the global mean coefficient reported in the literature. In this figure, it is possible to see that the CHIVO reflectivity deviates from the KuPR as the reflectivity gets higher values. The bias between KuPR reflectivity and CHIVO is 0.71 dB, the correlation coefficient is 0.94 and the RMSE is 2.4 dB in this case.

On the other hand, Fig. 9b shows the comparison using the local RELAMPAGO domain coefficient. In this figure, it can be seen that the CHIVO reflectivity matches well with KuPR reflectivity even for high values. The bias between KuPR reflectivity and CHIVO is 0.1 dB, the correlation coefficient is 0.95 and the RMSE is 2.35 dB in this case. A higher correlation and lower RMSE is observed when using the RELAMPAGO coefficient compared to the the results using the global coefficient. Similar results were also obtained with a different overpass on December 6th, 2018 for CHIVO. Table 3

Table 3 shows a summary of the cross-comparison of the RELAMPAGO GRs with KuPR using the RELAMPAGO coefficient. In the table, it is possible to see that CHIVO shows almost no bias with respect to KuPR for both of its overpasses. CSAPR shows a positive bias, which means that its reflectivity is slightly smaller than DPR. On the contrary, RMA shows a negative bias, which might indicate an overestimation of its reflectivity. It is worth mentioning that different GRs capture different overpasses. This difference might have an effect in the consistency of the comparison.

4.2 Inter-comparison of the ground radars

In this section, we present the results of the inter-comparison of the GRs used in our study. Similar to DPR cross-comparison, a better agreement between the radars was obtained using the RELAMPAGO coefficient. The inter-comparison is done for each pair of GRs, i.e., CHIVO vs CSAPR, CHIVO vs RMA, and RMA vs CSARP. Fig. 10

Figure 10 shows the scattergram of CHIVO and CSAPR reflectivity. Note that in the scattergram that CHIVO reflectivity seems to be slightly higher than CSAPR. Nevertheless, they compare well with a high correlation and low RMSE. Table 4

Table 4 shows the results for the rest of radars. The inter-comparison between CHIVO and RMA exhibits a negative bias. Which can be interpreted as a lower value in CHIVO reflectivity with respect to RMA. In the case of RMA vs CSAPR, the bias is now positive. Which means that RMA reflectivity is higher than CSAPR.

With the inter-comparison results, the question that arises is whether the GRs biases are consistent with the bias found with KuPR. The following section addresses this issue.

4.3 Bias consistency, analysis and estimation

In the last subsections, each radar is compared with one another. In total 4 radars are compared, including the KuPR. Tables 3 and 4 show the bias and correlation coefficient for the cross and inter comparison respectively. Nevertheless, we would like to know if the results are consistent between the different instrument. Therefore, we construct a visual representation in Fig. 11.

Figure 11 shows the results of the comparison in a directed graph. The vertices are the radars and the edges the comparison metrics. The edges show the bias in parenthesis and the correlation coefficient in square brackets. The direction of the arrows represents how the bias is computed, where the X radar is the beginning and the Y radar the end of the arrow. X and Y are specified as in the Eq. (6a). Since CHIVO had multiple overpasses, we average their biases and correlations to construct the KuPR-CHIVO edge. Fig. 11

The graph is arranged in the form of a triangular based pyramid. KuPR is placed in the apex of the pyramid because it is a common platform across the network of radars. In other words, KuPR is used as a reference in the space to bring the other corners of the pyramid together. The GRs are placed in the pyramid's base to represent that they are ground-based sensors.

To have an insight into the bias consistency, one can take a walk around one of the pyramid faces and add the biases. Let's call the result of this summation the residual bias (δB) from a face. For example, take the phase formed by CHIVO-RMA-CSAPR. In this case, the residual bias is:

$$\begin{aligned} \delta B &= B(CHIVO, RMA) + B(RMA, CSAPR) + B(CSAPR, CHIVO) \\ &= B(CHIVO, RMA) + B(RMA, CSAPR) - B(CHIVO, CSAPR) \\ &= (-0.95) + (1.91) - (1.31) = -0.35\,, \end{aligned} \tag{7}$$

where $B(Rd_X, Rd_Y)$ means the bias between the radar X and the Y. Note that $B(Rd_X, Rd_Y) = -B(Rd_Y, Rd_X)$ because the way the bias is defined. This is the reason why B(CSAPR, CHIVO) is replaced by -B(CHIVO, CSAPR) in the second line of Eq. (7).

Intuitively, the residual bias of a face should be equal to zero. The reason is that a radar's bias with itself is zero, or mathematically, $B(Rd_X, Rd_X) = 0$. Since one returns to the same radar after finishing a walk through the face, it is natural to expect that the biases compensate along the vertices and as a result the residual bias should be zero. For example, in the walk through CHIVO-RMA-CSAPR face, one starts with the bias from CHIVO to RMA and concludes with the bias from CSAPR to CHIVO (first line of Eq. (7)). Table 5

In this respect, computing the residual bias for each face can provide a sense of how consistent is the comparison between the radars. Table 5 shows the δB for each face of the graph in Fig. 11. The meaning of $\delta\tilde{B}$ in Table 5 will be explained later in this section. The residual biases are computed counter-clockwise in the direction specified by the order of the radar in the table. Note that a switch in the clockwise direction only changes the residual bias sign, but the magnitude remains constant.

From Table 5, one can see that the absolute maximum residual bias (max. $|\delta B|$) is 0.52 dB. This max. $|\delta B|$ can be interpreted as the comparison of each sensor to one another is consistent within half of dB. More about this interpretation is expanded in the discussion section.

Moreover, this confirms that we can use KuPR to bring the network of GRs into better agreement. A new bias between each pair of radars is recomputed. The new bias is found by averaging the sum of biases from the paths that connect two radars in the graph. The averaging is weighted using the correlation coefficient. When a path has more than one edge, the correlation coefficient is found by multiplying the individual correlations.

For instance, to go from CHIVO to CSAPR, one can go directly, through KuPR, or through RMA. We did not include paths that have more than one radar in between e.g. CHIVO-RMA-KuPR-CSAPR. The reason is because they can induce more uncertainty in the estimation. Hence, the path's biases for the CHIVO and CSAPR example are given by:

$$B(CHIVO, CSAPR|KuPR) = B(CHIVO, KuPR) + B(KuPR, CSAPR),$$
$$B(CHIVO, CSAPR|RMA) = B(CHIVO, RMA) + B(RMA, CSAPR), \quad (8)$$

where $B(Rd_X, Rd_Y|Rd_Z)$ is the sum of biases in the path that connect the radar X and Y passing through the radar Z.

Similarly, the correlation of the path that connect the radar X with Y passing through the radar Z can be defined as:

$$Corr(Rd_X, Rd_Y|Rd_Z) = Corr(Rd_X, Rd_Z) \times Corr(Rd_Z, Rd_y). \quad (9)$$

In this way, the correlation of the paths that goes from CHIVO to CSAPR are given by:

$$Corr(CHIVO, CSAPR|KuPR) = Corr(CHIVO, KuPR) \times Corr(KuPR, CSAPR),$$
$$Corr(CHIVO, CSAPR|RMA) = Corr(CHIVO, RMA) \times Corr(RMA, CSAPR). \quad (10)$$

Table 6

Table 6 shows the numeric values of the paths' bias and correlation that connects CHIVO and CSAPR. As expected, the direct path that connects CHIVO and CSAPR has the highest correlation because it doesn't go through any other radars. However, the smaller biases going through KuPR and RMA suggest that the bias between CHIVO and CSAPR should be lower than the bias computed directly. Therefore, it makes sense to compute a new bias combining the biases from different paths. The correlation can be used to weight the bias.

In the case of CHIVO and CSAPR, the bias can be recalculated as follows:

$$\begin{aligned}
&\tilde{B}(CHIVO, CSAPR) = \\
&[B(CHIVO, CSAPR) \times Corr(CHIVO, CSAPR) + \\
&B(CHIVO, CSAPR|KuPR) \times Corr(CHIVO, CSAPR|KuPR) + \\
&B(CHIVO, CSAPR|RMA) \times Corr(CHIVO, CSAPR|RMA)]/ \\
&[Corr(CHIVO, CSAPR) + Corr(CHIVO, CSAPR|KuPR) + \\
&Corr(CHIVO, CSAPR|RMA)],
\end{aligned} \tag{11}$$

where $\tilde{B}(Rd_X, Rd_Y)$ is the estimation of the new bias between the radar X and Y.

In a similar way, the new biases are computed for the other edges of the graph and they are shown in Fig. 12. Table 5 shows the new residual bias ($\delta\tilde{B}$) for the faces of the graph in Fig. 12. Note that the the absolute maximum residual bias (max. $|\delta\tilde{B}|$) is 0.17 dB for Fig. 12 graph. This reduction in the max. $|\delta\tilde{B}|$ compared to the max. $|\delta B|$ from Fig. 11 can be interpreted as the new estimated biases are in better agreement in the network. Fig. 12

5. Discussion

A discussion of the main results in this study is presented. First, the increase in the α-value in the RELAMPAGO domain is examined. Second, the residual bias as a measurement of the consistency of the bias in a radar network is explained. Finally, a procedure to find a more consistent bias between the network of radars is discussed.

We found a change in the α-value derived from the local disdrometer in the RELAMPAGO domain compared to the α-value reported by Bringi and Chandrasekar (2001), that was derived from a global set of DSDs. A comparison with KuPR suggests a better agreement using the RELAMPAGO α-value for the GR's attenuation correction. Almost a one-to-one agreement was observed for CHIVO using the RELAMPAGO coefficient. The results shown in Fig. 9 suggests that the higher the reflectivity, the lower the agreement for the global average coefficient.

The change in the RELAMPAGO α-value is due to the narrower domain of DSD for the local region. The RELAMPAGO domain is known for having some of the most intense convection on earth. Disdrometer analysis shown by Rivelli Zea (2020) reveals an increase in the normalized droplet concentration in the RELAMPAGO domain. This variation in the DSD in the RELAMPAGO domain makes more relevant the computation of the attenuation coefficients for this region.

The graphical representation shown in Fig. 11 helps to have a better interpretation of the results. For example, CHIVO shows a good agreement with KuPR with a high correlation within 0.9 and almost unbiased reflectivity. CSAPR and RMA also compare well with KuPR with correlation within 0.8 and around 1 dB bias. CHIVO also compares well with CSAPR and RMA with a high correlation within 0.85. The slightly low correlation between RMA and CSAPR was expected because the distance between these two radars is the longest.

The graph in Fig. 11 also suggests the residual bias's computation as shown in Eq. (7) for CHIVO-RMA-CSAPR face. The residual bias along the faces of the graph provides a sense of the consistency of the comparison. Ideally, the residual bias should be zero. An intuitive explanation is because in a close path one returns back to the starting point. As a result, δB can be seen as the "boundary condition", as instrument's bias with itself, i.e., zero.

As shown in Table 5, the maximum absolute residual bias in Fig. 11 is about half of dB. The max. $|\delta B|$ can be seen as a measurement of the bias consistency between different instruments. The reason is that each δB represents how consistent is the bias between three of the sensors. The results show a max. $|\delta B|$ of half of dB, which can be interpreted as the mean uncertainty of the radars' comparison.

A method to find a more consistent bias in the graph is proposed. The bias between two radars is combined with the bias going through the other two radars in the graph. An example to compute a new bias between CHIVO and CSAPR using the information from KuPR and RMA is presented in Eq. (11). The same procedure is applied to the other radars in the network, including KuPR.

The values of the new biases are presented in Fig. 12. The residual bias is found for the faces of the new graph, and it is shown in Table 5 in the $\delta\tilde{B}$ column. Note that there is a reduction in the residual bias for the recalculated graph. The lower $\delta\tilde{B}$ can be interpreted as the biases in the graph are more consistent between the different nodes.

6. Summary and Conclusions

We present an intercomparison of three radars with KuPR in this study. The intercomparison is done using the network of C-band radars deployed during the RELAMPAGO field campaign in Argentina. We also compare the GRs between each other. Each instrument is compared pairwise with one another, including KuPR. Evaluating the network consistency in itself is the unique aspect of this paper, in addition to the comparison with KuPR.

Attenuation correction coefficients were computed from DSD measured by disdrometer deployed in the GRs domain during the field campaign to improve the accuracy of attenuation corrected reflectivity. The derived coefficients were slightly higher than the global average values reported in the literature. The bias between KuPR and the GRs reduces when the RELAMPAGO coefficients are used to correct attenuation.

We propose a method to evaluate the consistency of the bias in the network of GRs and KuPR. Previous studies compare each GR with KuPR individually. The GRs used in this study were located such that there was enough overlapping coverage regions that allowed performing comparison between them. Therefore, we were able to compute the bias between each pair of instruments. The residual bias between three of the radars is used to have a sense of the biases' consistency. We also propose a method to compute a more consistent bias between two radars employing the other instruments' information.

Acknowledgements

This study is supported by the USA National Science Foundation (NSF). The authors would like to thank to all the RELAMPAGO team for the effort to collect this outstanding data set, and the DOE ARM and CSAPR team for the CSAPR data set. RMA-1 is provided by Secretaria de Infraestructura y Politica Hidrica, Ministerio de Obras Publicas of the Argentinean National Government and INVAP S.E. framed within the SINARAME Project. The National System of Weather Radars (Sistema Nacional de Radares Meteorológicos, SINARAME) project is an Argentinean effort to expand the radar network over the whole country.

The authors would like to acknowledge Prof. Stephen Nesbitt and his group at the University of Illinois for discussions related to using disdrometer derived coefficients.

The authors would like to acknowledge to two anonymous reviewers for their valuable comments and suggestions.

References

Anagnostou, E. N., C. A. Morales, and T. Dinku, 2001: The use of TRMM precipitation radar observations in determining ground radar calibration biases. *J. Atmos. Oceanic Technol.*, **18(4)**, 616–628.

Bartholomew, M. J., 2020: Two-Dimensional Video Disdrometer (VDIS) Instrument Handbook. Technical report, DOE Office of Science Atmospheric Radiation Measurement (ARM) Program, 18.

Biswas, S. K., and V. Chandrasekar, 2018: Cross-validation of observations between the GPM dual-frequency precipitation radar and ground based dual-polarization radars. *Remote Sens.*, **10(11)**, 1773.

Bolen, S. M., and V. Chandrasekar, 2000: Quantitative cross validation of space-based and ground-based radar observations. *J. Appl. Meteor.*, **39(12)**, 2071–2079.

Bolen, S. M., and V. Chandrasekar, 2003: Methodology for aligning and comparing spaceborne radar and ground-based radar observations. *J. Atmos. Oceanic Technol.*, **20(5)**, 647–659.

Bringi, V. N., and V. Chandrasekar, 2001: *Polarimetric Doppler weather radar: principles and applications*. Cambridge University Press, 493.

Hou, A. Y., R. K. Kakar, S. Neeck, A. A. Azarbarzin, C. D. Kummerow, M. Kojima, R. Oki, K. Nakamura, and T. Iguchi, 2014: The global precipitation measurement mission. *Bull. Amer. Meteor. Soc.*, **95(5)**, 701–722.

Iguchi, T., 2020: Dual-Frequency Precipitation Radar (DPR) on the Global

Precipitation Measurement. *Satellite Precipitation Measurement: Volume 1*, **67**, 183.

Kanemaru, K., T. Iguchi, T. Masaki, and T. Kubota, 2020: Estimates of spaceborne precipitation radar pulsewidth and beamwidth using sea surface echo data. *IEEE Trans. Geosci. Remote Sens.*, **58(8)**, 5291–5303.

Kojima, M., T. Miura, K. Furukawa, Y. Hyakusoku, T. Ishikiri, H. Kai, T. Iguchi, H. Hanado, and K. Nakagawa, 2012: Dual-frequency precipitation radar (DPR) development on the global precipitation measurement (GPM) core observatory. In *Earth observing missions and sensors: Development, implementation, and characterization II*, Volume 8528, International Society for Optics and Photonics, 85281A.

Kozu, T., T. Kawanishi, H. Kuroiwa, M. Kojima, K. Oikawa, H. Kumagai, K. Okamoto, M. Okumura, H. Nakatsuka, and K. Nishikawa, 2001: Development of precipitation radar onboard the tropical rainfall measuring mission (trmm) satellite. *IEEE Trans. Geosci. Remote Sens.*, **39(1)**, 102–116.

Kummerow, C., W. Barnes, T. Kozu, J. Shiue, and J. Simpson, 1998: The tropical rainfall measuring mission (TRMM) sensor package. *J. Atmos. Oceanic Technol.*, **15(3)**, 809–817.

Louf, V., A. Protat, R. A. Warren, S. M. Collis, D. B. Wolff, S. Raunyiar, C. Jakob, and W. A. Petersen, 2019: An integrated approach to weather radar calibration and monitoring using ground clutter and satellite comparisons. *J. Atmos. Oceanic Technol.*, **36(1)**, 17–39.

Masaki, T., T. Iguchi, K. Kanemaru, K. Furukawa, N. Yoshida, T. Kubota, and R. Oki, 2020: Calibration of the dual-frequency precipitation radar onboard the Global Precipitation Measurement Core Observatory. *IEEE Trans. Geosci. Remote Sens.*

Rasmussen, K. L., and R. A. Houze, 2011: Orogenic convection in subtropical South America as seen by the TRMM satellite. *Mon. Wea. Rev.*, **139(8)**, 2399–2420.

Rasmussen, K. L., and R. A. Houze, 2016: Convective initiation near the Andes in subtropical South America. *Mon. Wea. Rev.*, **144(6)**, 2351–2374.

Rivelli Zea, L. E., 2020: RELAMPAGO-CACTI drop size distribution observations and the implications for cloud and hydrologic studies. Master's thesis, Univeristy of Illinois, 52.

Schwaller, M. R., and K. R. Morris, 2011: A ground validation network for the global precipitation measurement mission. *J. Atmos. Oceanic Technol.*, **28(3)**, 301–319.

Seto, S., T. Iguchi, R. Meneghini, J. Awaka, T. Kubota, T. Masaki, and N. Takahashi, 2021: The precipitation rate retrieval algorithms for the GPM Dual-frequency Precipitation Radar. *J. Meteor. Soc. Japan*, **99(2)**, 205–237.

Skofronick-Jackson, G., W. A. Petersen, W. Berg, C. Kidd, E. F. Stocker, D. B. Kirschbaum, R. Kakar, S. A. Braun, G. J. Huffman, T. Iguchi, and others, 2017: The global precipitation measurement (GPM) mission for science and society. *Bull. Amer. Meteor. Soc.*, **98(8)**, 1679–1695.

Warren, R. A., A. Protat, S. T. Siems, H. A. Ramsay, V. Louf, M. J. Manton, and T. A. Kane, 2018: Calibrating ground-based radars against TRMM and GPM. *J. Atmos. Oceanic Technol.*, **35(2)**, 323–346.

Zipser, E. J., D. J. Cecil, C. Liu, S. W. Nesbitt, and D. P. Yorty, 2006: Where are the most intense thunderstorms on earth? *Bull. Amer. Meteor. Soc.*, **87(8)**, 1057–1072.

List of Figures

Fig. 1: CSU-CHIVO deployed south of Cordoba City, Argentina, during RELAMPAGO.

Fig. 2: ARM mobile facility deployed during CACTI-RELAMPAGO. Sensors left to right: Sonic Detection and Ranging wind profiler (SODAR), C-band Scan Precipitation Radar 2 (CSAPR-2), X and Ka band Scan ARM Cloud Radars (XSACR and KaSACR), and Ka-band Zenith Radar (KAZR).

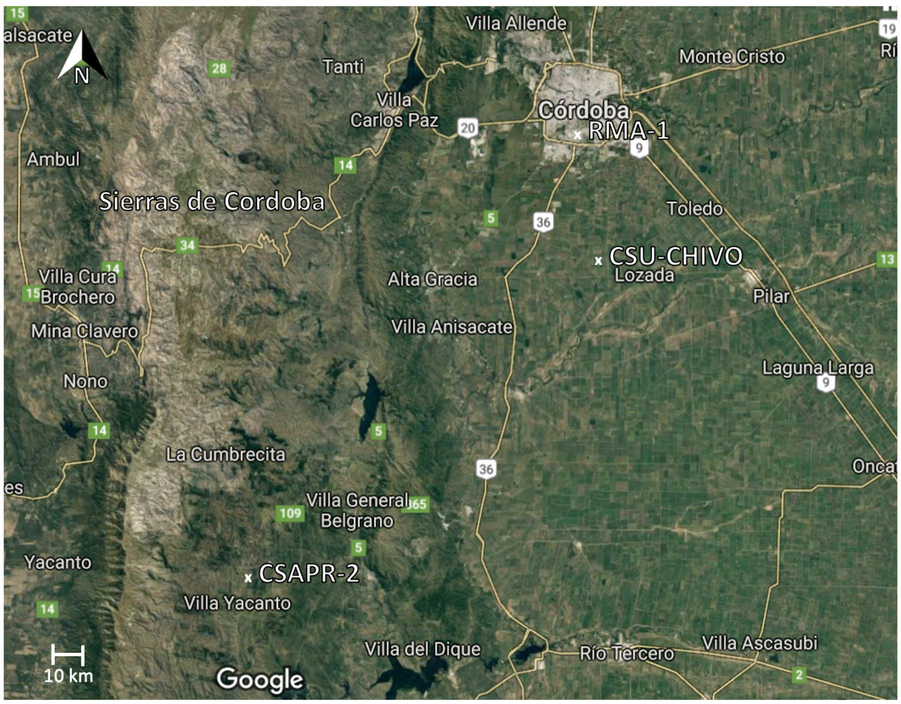

Fig. 3: Map with the locations of the network of C-band radars during the RELAMPAGO campaign (CSU-CHIVO, CSAPR-2, and RMA-1).

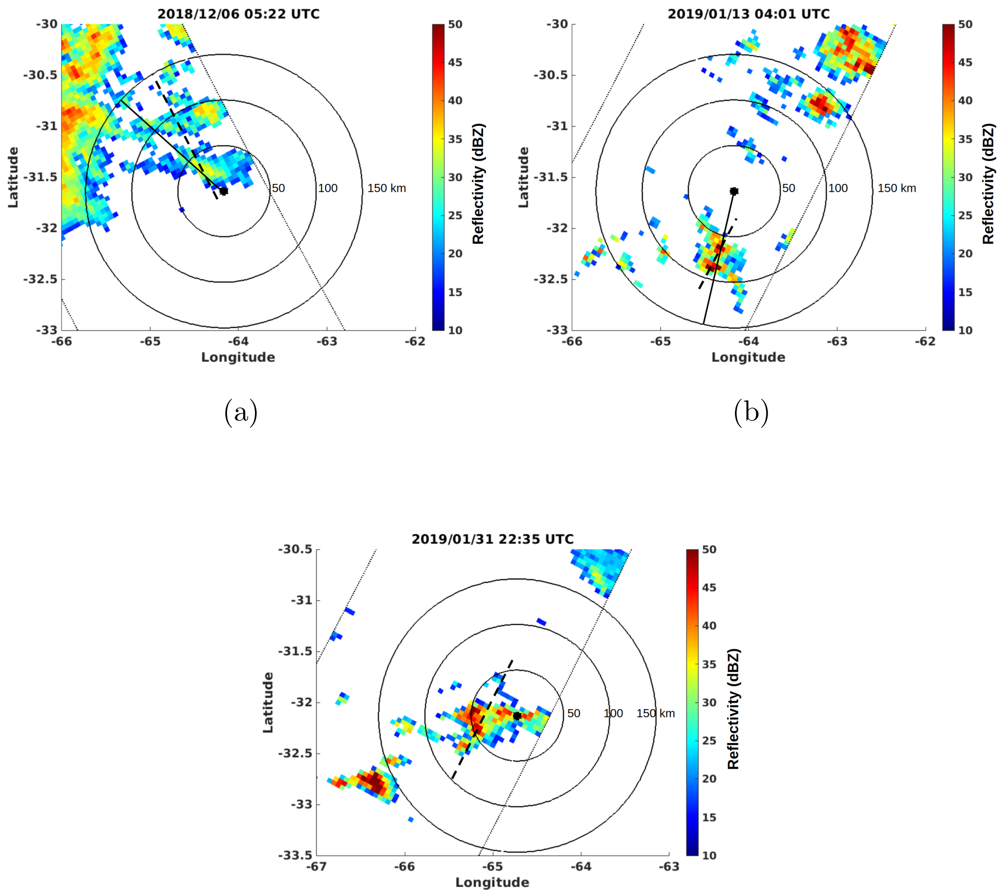

(a) (b) (c)

Fig. 4: KuPR reflectivity at 2 km altitude on (a) December 6th, 2018 at 05:22 UTC, (b) January 13th, 2019 at 4:01 UTC, and (c) January 31st, 2019 at 22:35 UTC. The solid line in (a), and (b) indicates CHIVO RHI along 315°, and 192° azimuth respectively. The dashed line in (a), (b), and (c) denotes KuPR angle bins 39, 13, and 37 respectively. The doted lines represents the edges of the KuPR swath. The rings in (a), and (b) are centered at CHIVO, whereas for (c) are centered at CSAPR.

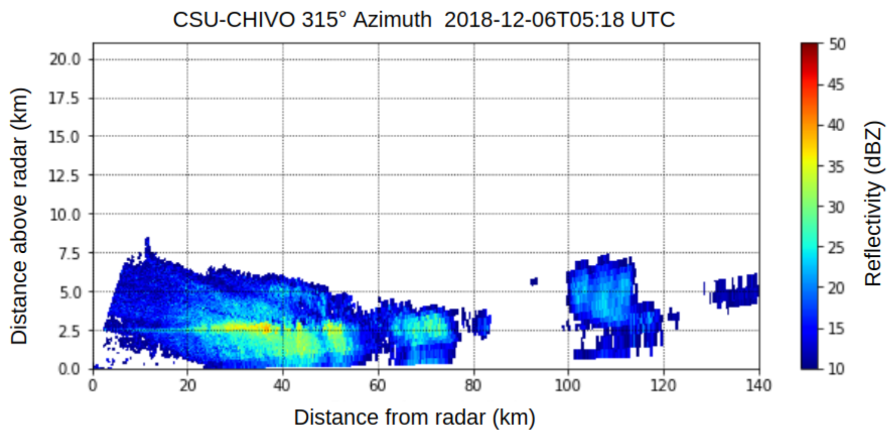

(a)

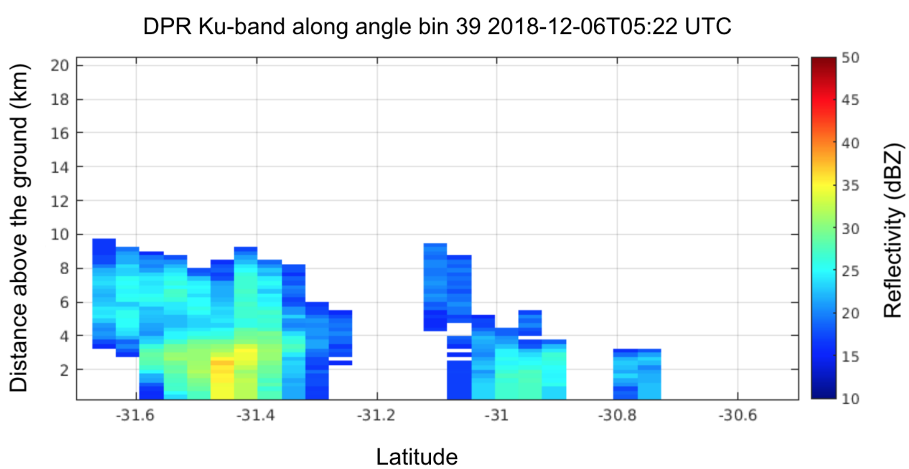

(b)

Fig. 5: December 6th, 2018 reflectivity from: (a) CHIVO RHI along 315° azimuth at 05:18 UTC, and (b) KuPR along angle bin 39 at 05:22 UTC. The CHIVO RHI and DPR angle bin are marked by the solid and the dashed line in Fig. 4a.

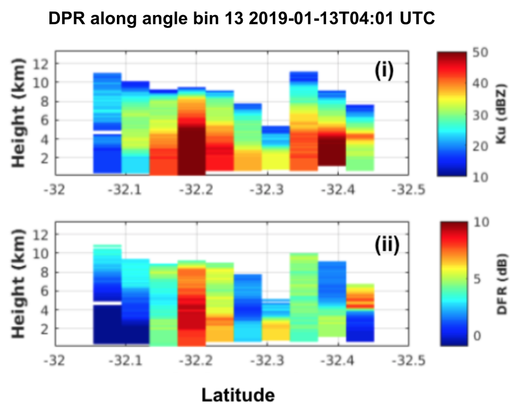

(a)

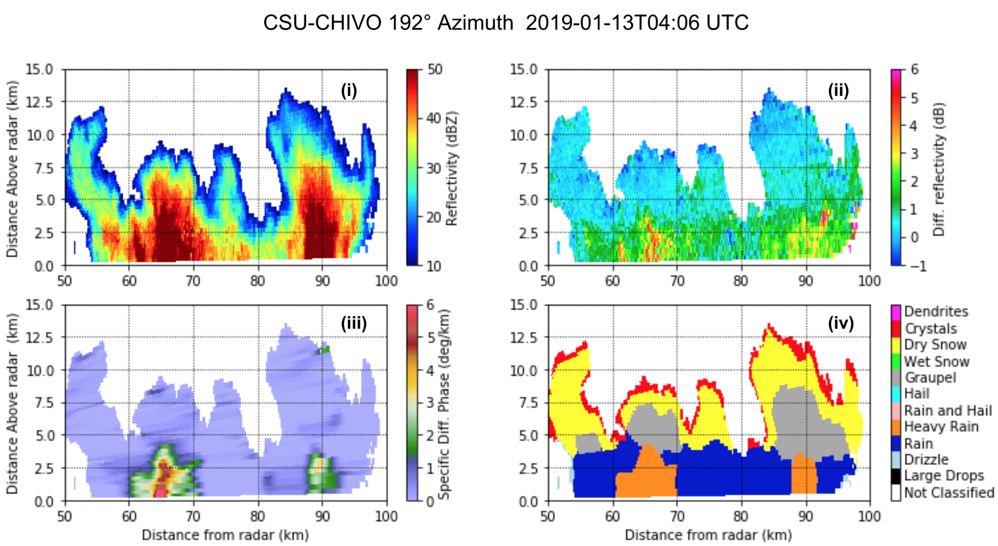

(b)

Fig. 6: January 13th, 2019. (a): DPR along angle bin 13 at 4:01 UTC, Ku-band reflectivity (i), and Dual Frequency Ratio (DFR) (ii). (b): CHIVO RHI along 192° azimuth at 4:06 UTC, reflectivity (i), differential reflectivity (ii), specific differential phase (iii), and hydrometeor classification (iv).

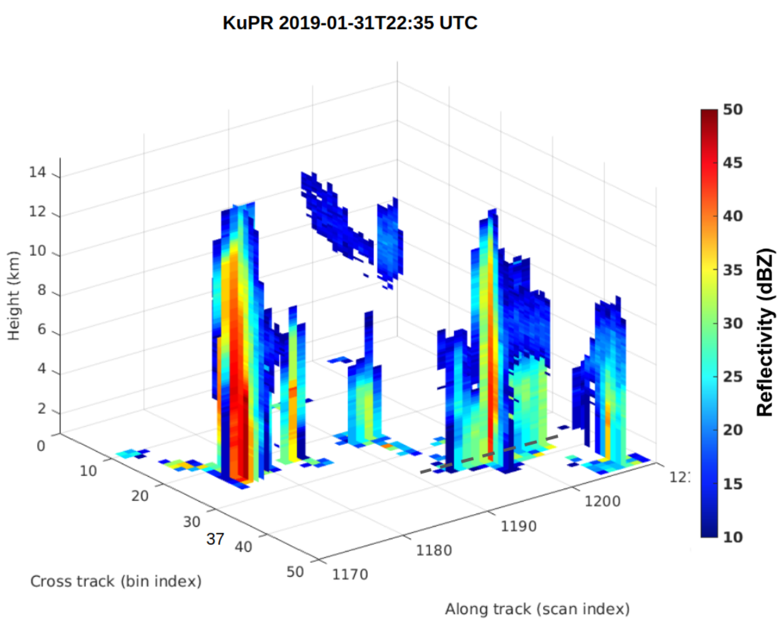

Fig. 7: KuPR reflectivity on January 31st, 2019 at 22:35 UTC, 3D depiction.

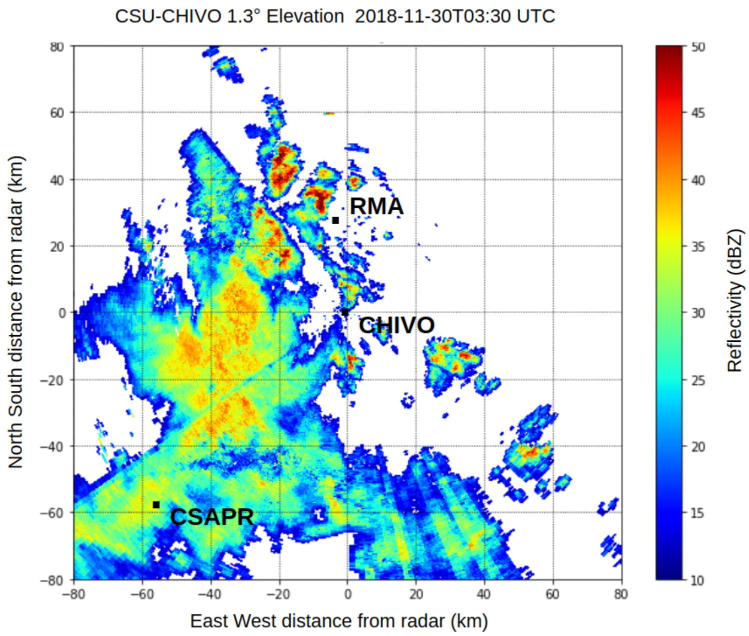

(a)

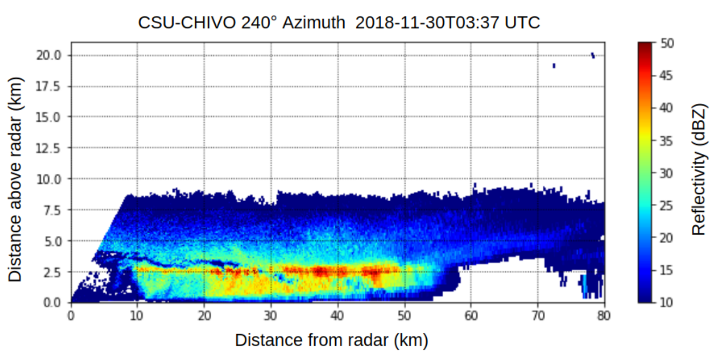

(b)

Fig. 8: CHIVO reflectivity on November 30th, 2018. (a) PPI scan at 3:30 UTC, and (b) RHI scan at 3:37 UTC.

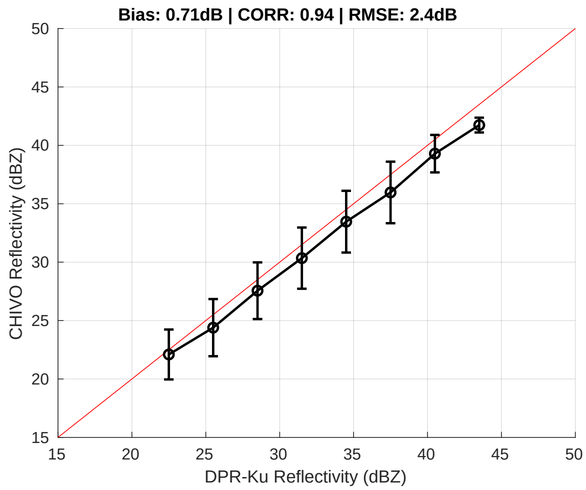

(a)

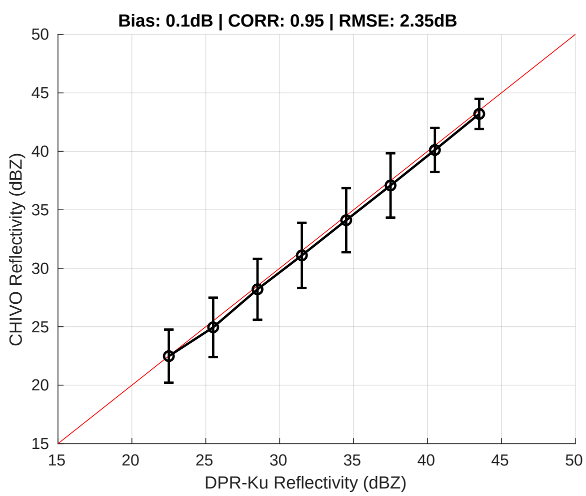

(b)

Fig. 9: CSU-CHIVO and KuPR reflectivity comparison for January 13, 2019 case at 4:02 UTC. CHIVO reflectivity is corrected for attenuation using (a) global average coefficient, and (b) coefficient computed from the disdrometer in the field. The dots represent the mean and bars one standard deviation.

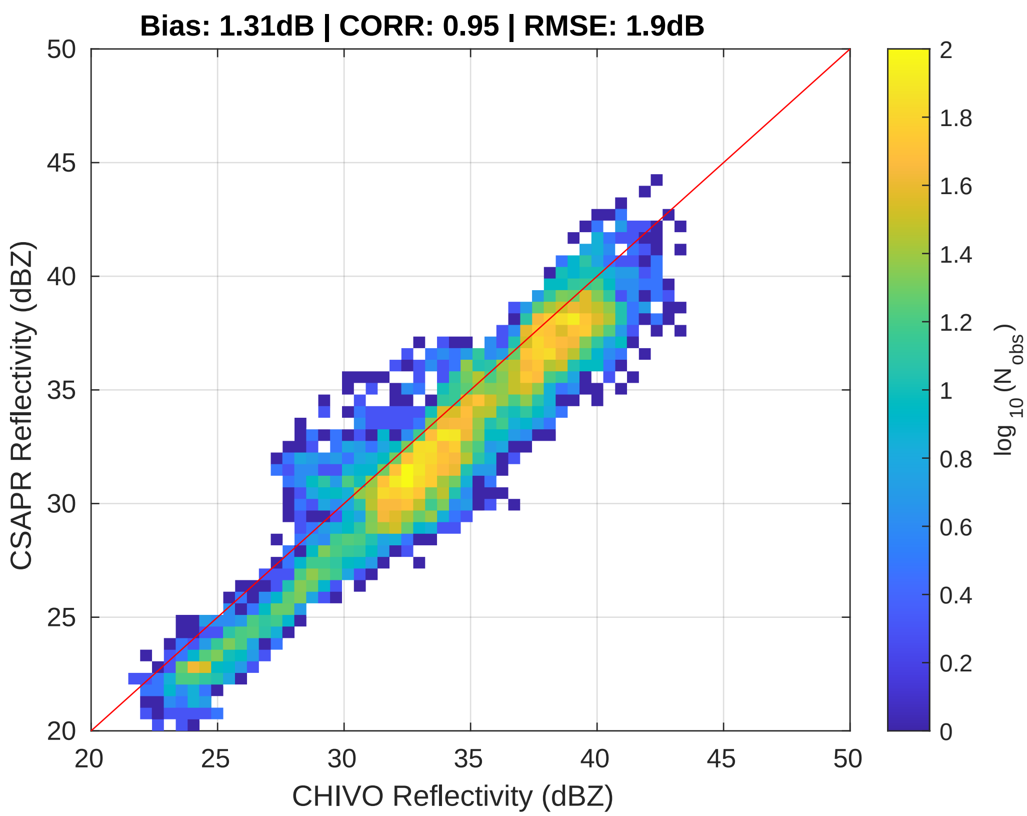

Fig. 10: CSAPR-2 and CSU-CHIVO reflectivity comparison for November 30th, 2018 case at 3:30 UTC. CSAPR and CHIVO reflectivities are corrected for attenuation using coefficient computed from the disdrometer in the field.

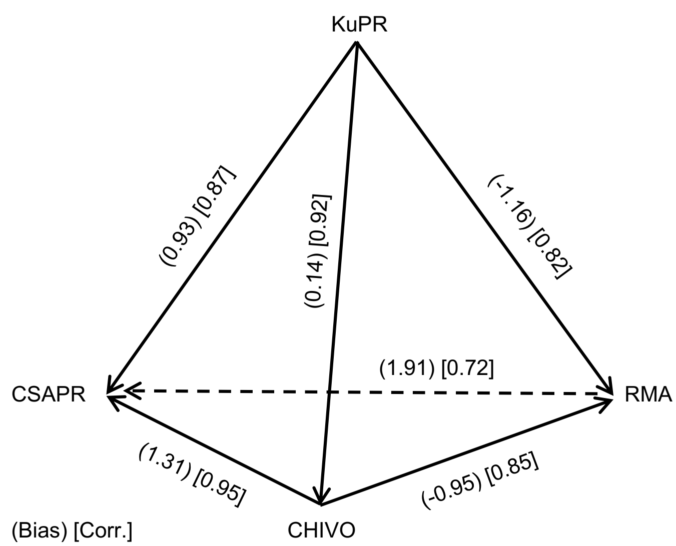

Fig. 11: Bias (parenthesis, dB) and correlation coefficient (square brackets) from the cross and inter comparison. The arrows indicate the direction in which the bias is computed, being X the beginning and Y the end of the arrow.

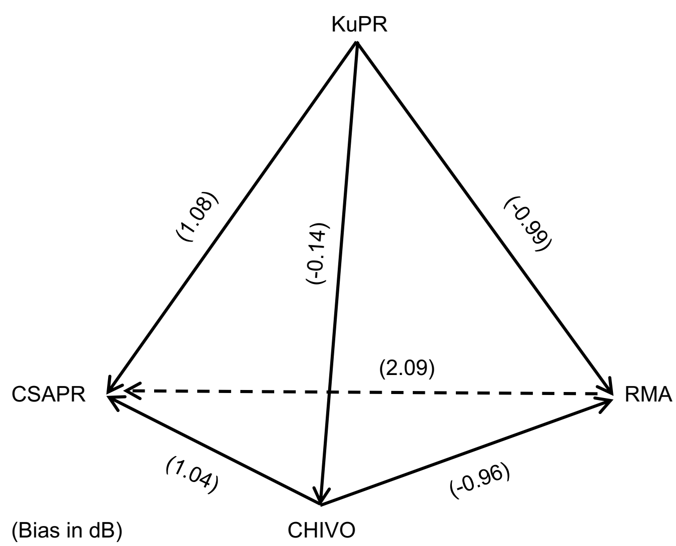

Fig. 12: Recalculated bias using the information from the other path as in Eq. (11), the arrows are defined as in Fig. 11.

List of Tables

Table 1: List of GPM DPR overpasses during RELAMPAGO with significant weather. The Radar column means the GRs that capture the overpass with a good alignment in time and space with GPM DPR.

Date	**Time (UTC)**	**Radar**
2018/12/06	05:22	CHIVO/RMA
2019/01/13	04:01	CHIVO
2019/01/31	22:35	CSAPR

Table 2: Resolution of space and ground-based radar used in this study.

Radar	**Beam-width (deg.)**	**Pulse duration (μs)**	**Range resolution (m)**	**Footprint**
KuPR	0.72	1.6/3.2	250/500	5 km at 400km
CSU-CHIVO	0.95	1.0	150	994 m at 60 km
CSAPR-2	0.90	0.7	100	942 m at 60 km
RMA-1	0.87	3.0	450	911 m at 60 km

Table 3: Summary of the cross-comparison with KuPR of the ground-based radars during RELAMPAGO. The time is for the overpass. The bias, correlation coefficient, and RMSE are computed as defined in the set of Eq. (6) where Rd_X is KuPR and Rd_Y is the GR. The Samples column refers to the number of points used in the comparison.

Date	**Time (UTC)**	**Radar**	**Bias (dB)**	**Corr.**	**RMSE (dB)**	**Samples**
2018/12/06	05:22	CHIVO	0.17	0.89	1.94	776
		RMA	-1.16	0.82	3.01	1104
2019/01/13	04:01	CHIVO	0.10	0.95	2.35	458
2019/01/31	22:35	CSAPR	0.93	0.87	3.04	946

Table 4: Summary of the inter-comparison between the ground-based radar on November 30th, 2018 case. The bias, correlation coefficient and, RMSE are computed as defined in the set of Eq. (6) where the order of radars are given by Rd_X vs. Rd_Y in the Radars column. The Samples column refers to the number of points used in the comparison.

Time (UTC)	**Radars**	**Bias (dB)**	**Corr.**	**RMSE (dB)**	**Samples**
3:30	CHIVO vs. CSAPR	1.31	0.95	1.90	7772
4:00	CHIVO vs. RMA	-0.95	0.85	2.57	7791
3:15	RMA vs. CSAPR	1.91	0.72	3.95	7539

Table 5: Residual bias (δB) for the faces of the graph in Fig. 11, and residual recalculated bias ($\delta \tilde{B}$) of the graph in Fig. 12.

Face	$\delta B(dB)$	$\delta \tilde{B}(dB)$
CHIVO-RMA-CSAPR	-0.35	0.09
CHIVO-RMA-KuPR	0.35	-0.11
CHIVO-KuPR-CSAPR	-0.52	0.17
KuPR-CSAPR-RMA	0.18	-0.03

Table 6: From CHIVO to CSAPR, biases using different path. Bias is computed as shown in Eq. (8) where Rd_X is CHIVO, Rd_Y is CSAPR.

Path	**Bias (dB)**	**Corr.**
CHIVO-CSAPR	1.31	0.95
CHIVO-KuPR-CSAPR	0.79	0.80
CHIVO-RMA-CSAPR	0.96	0.61